Caged-cations-induced Lattice Distortion in Bronze TiO_2 for Cohering Nanoparticulate Hydrogen-evolution Electrocatalysts

Gaoxin Lin[ab], Qiangjian Ju[ab], Lijia Liu[c], Xuyun Guo[d], Ye Zhu[d], Zhuang Zhang[ab], Chendong Zhao[ab], Yingjie Wan[ab], Minghui Yang,[e] Fuqiang Huang[af]*, Jiacheng Wang[ab]*

[a]State Key Lab of High Performance Ceramics and Superfine microstructure, Shanghai Institute of Ceramics, Chinese Academy of Sciences, Shanghai 201899, China.

[b]Center of Materials Science and Optoelectronics Engineering, University of Chinese Academy of Sciences, Beijing 100049, China.

[c]Department of Chemistry, Western University, 1151 Richmond Street, London, ON N6A5B7, Canada.

[d]Department of Applied Physics, Research Institute for Smart Energy, The Hong Kong Polytechnic University, Hung Hom, Kowloon, Hong Kong, China.

[e]School of Environmental Science and Technology, Dalian University of Technology, Dalian, Liaoning 116024, China

[f]State Key Laboratory of Rare Earth Materials Chemistry and Applications, College of Chemistry and Molecular Engineering, Peking University, Beijing 100871, China.

Email: huangfq@mail.sic.ac.cn; jiacheng.wang@mail.sic.ac.cn

Keywords: Caged cations; Lattice distortion; Bronze TiO_2; Synergistic effect; Electrocatalysis

Abstract

Defect engineering provides a promising approach for optimizing the trade-off between support structures and active nanoparticles in heterojunction nanostructures, manifesting efficient synergy in advanced catalysis. Herein, high-density of distorted lattices and defects are successfully formed in bronze TiO_2 through caging alkali-metal Na cations in open voids (Na-TiO_2(B)), which could efficiently cohere nanoparticulate electrocatalysts toward alkaline hydrogen evolution reaction (HER). The RuMo bimetallic nanoparticles could directionally anchor on Na-TiO_2(B) with a certain angle

of ~22° due to elimination of lattice mismatch, thus promoting uniform dispersion and small sizing of supported nanoparticles. Moreover, caging Na ions could significantly enhance the hydrophilia of the substrate in RuMo/Na-TiO_2(B), leading to the strengthening synergy of water dissociation and hydrogen desorption. As expected, this Na-caged nanocomposite catalyst rich with structural perturbations manifests a factor of 6.4 times turnover frequency (TOF) increase compared to Pt/C. The study provides a new paradigm for designing stable nano-heterojunction catalysts with lattice-distorted substrate *via* caging cations toward advanced electrocatalytic transformations.

1. Introduction

The heterojunction nanostructures are considered to promote the advancement of highly active electrocatalysts due to their unique physicochemical properties[1]. The well-defined functions in composites lead to better catalytic activity compared to the simple summary of individual components due to the increased active sites and improved intrinsic activity[2]. However, the trade-off produced by the interaction of surface structure and catalytic activity in heterojunction nanostructures requires to be optimized[3]. Defect engineering has emerged as an efficient method to coordinate the physicochemical properties of each component in heterojunction nanostructures and expert a positive impact on electrocatalysis[4]. The defects including vacancy, edge dislocation, grain boundary and spatial lattice disorder can act as the atomic interface with unsaturated coordination and electronic delocalization to moderate the binding energy of chemical reactants, thereby enhancing the catalytic activity[5]. For example, the grain boundaries and surface strain in Pt/Al_2O_3 composite catalysts exhibited a concerted effect in oxygen dissociation and C–H activation, resulting in at least a two-fold enhancement in catalytic activity[6]. Therefore, rational fabrication of heterojunction nanostructure with defect engineering is attractive to develop high performance electrocatalysts.

Alkali-metal ions adsorption on the defined surface of composites is a facile method to produce the defects and enhance catalytic activity[7]. The localized defects with alkali-metal ions can serve as electronic or textural promoters of catalysts by

electronic interaction, site-blocking effect or surface reconstruction[8]. Though the alkali-metal decorated substrate was confirmed to control morphology and enhance stability of loaded nanoparticles[9], their own catalytic ability was generally ignored, which may facilitate the concerted effect on the multi-step catalytic reactions. And alkali-metal ions tend to be enriched on the surface of substrate in the form of hydrated ions[7a, 10], which can hardly activate the bulk structure to smooth the electrocatalysis with synergistic effect.

Herein, the bronze TiO_2 nanobelts with caged Na cations (Na-TiO_2(B)) have been prepared for constructing nanosized heterojunctions by cohering small-size RuMo nanoparticles, possessing the synergistic active sites for boosting alkaline HER (Figure 1). TiO_2(B) with bridge-oxygen linked octahedra provides open voids and parallel channels for caging Na^+ (Figure 1a), which leads to the structural perturbation and lattice distortion of nanobelts. The caged Na^+ also benefits the water adsorption and bubble removal of the substrate as the water contact angle sharply decreases to 10.6° (Figure 1c). And the defects serve as active sites for directionally anchored RuMo nanoparticle with a uniform size distribution of 2.1 ± 0.4 nm, much smaller than that on the substrate without caged Na^+ (3.0 ± 0.9 nm) (Figure 1d). Therefore, the catalyst exhibits a low Tafel slope of 19.2 mV dec^{-1} and high turnover frequency (TOF) of 0.71 H_2 s^{-1} (at an overpotential of 40 mV, Figure 1e), which is 6.4 times than that of commercial Pt/C. The concerted effect is proposed by the comparison of alkaline and acid HER activity: Na^+ modified substrate facilitates the water adsorption and H–OH bond cleavage, while RuMo alloy is responsible for the hydrogen desorption.

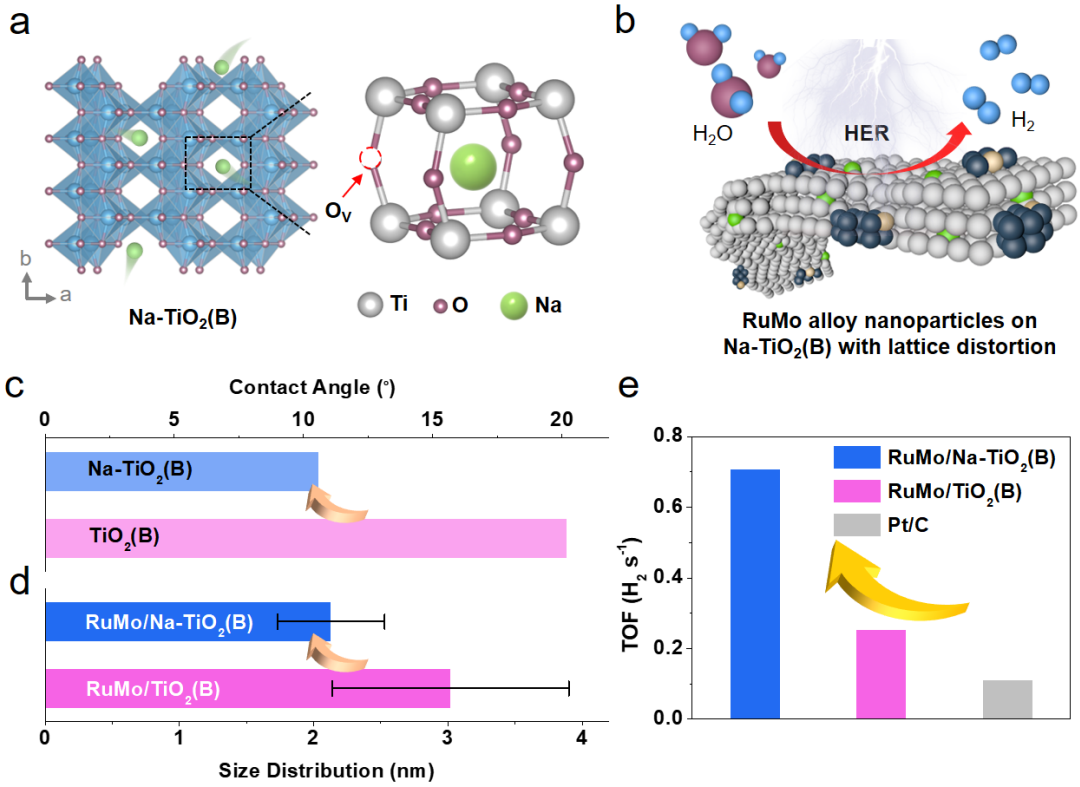

Figure 1. (a) Structural illustrations of bronze TiO_2 with caged Na cations (Na-TiO_2(B)). The open voids in TiO_2(B) provide connected channels for caging Na cations. (b) Schematic drawing of RuMo alloy nanoparticles strongly cohered on Na-TiO_2(B) with distorted lattices (RuMo/Na-TiO_2(B)) toward efficient HER. (c) Comparison of water contact angle values between Na-TiO_2(B) and TiO_2(B), and (d) RuMo particle size distribution between RuMo/Na-TiO_2(B) and RuMo/TiO_2(B). (e) Comparison of TOF values for RuMo/Na-TiO_2(B), RuMo/TiO_2(B) and commercial Pt/C at an overpotential of 40 mV toward alkaline HER.

2. Results and Discussion

2.1 Structural characterization of RuMo/Na-TiO_2(B)

RuMo/Na-TiO_2(B) with nanobelt-like morphology was synthesized by liquid phase reduction of ruthenium and molybdenum salts in a suspension of $H_2Ti_3O_7$ nanobelts with the assistance of sodium borohydride, followed by annealing in H_2/Ar (10% H_2) atmosphere. In the meantime, Na^+ from sodium borohydride could exchange with partial H^+ of $H_2Ti_3O_7$, inducing structural perturbation of the Ti–O cages in Na-

TiO_2(B) after dehydration. The X-ray diffraction (XRD) patterns show the monoclinic structure of TiO_2(B)[11] (Figure 2a). In RuMo/Na-TiO_2(B), most of diffraction peaks corresponding to TiO_2(B) weakened, which are attributed to structural defects and lattice distortion. And the perturbation degree increases with the caged Na^+ content (Figure S1). The electron paramagnetic resonances (EPR) spectra were collected to evaluate the oxygen vacancy (O_V) in the samples, and the symmetric Lorentzian lines with a *g* value of 2.004 was obtained (Figure 2b) [12]. The caged metal cations could facilitate the generation of O_V as the EPR intensity increased from TiO_2(B) to Na-TiO_2(B) and to RuMo/Na-TiO_2(B). It is also consistent with the result of O1s X-ray photoelectron spectroscopy (XPS) spectra. The increased content of peak at 532.3 eV suggests the generation of O_V (Figure S2)[13]. The presence of O_V was also confirmed by the extended X-ray absorption fine structure (EXAFS). Figure 2c exhibits two kinds of the Ti–O scattering paths at 1.10 Å for Ti–O (1) and 1.53 Å for Ti–O (2), corresponding to the bond lengths of 1.44 and 1.97 Å (Table S1), respectively. Compared to pristine Na-free TiO_2(B) with low density of O_V, the intensity of Ti–O (2) for RuMo/Na-TiO_2(B) decreases, suggesting the existence of high-density O_V. The increased O_V contents could promotes high electron concentration and improve the electric conductivity in the one-dimensional Na-TiO_2(B) nanobelts, favoring the fast electron transfer during electrocatalysis[14]. This is further proved by the conductivity measurements by the four-probe method. The results show that the conductivity of Na-TiO_2(B) with high lattice distortion is 2.07 μS cm^{-1}, two orders of magnitude higher than that of pristine Na-free TiO_2(B) (Figure S3).

The scanning electron microscopy images indicate the maintenance of nanobelt morphology after ion exchange, particles anchoring and pyrolysis (Figures S4-S6). The transmission electron microscopy (TEM) image for RuMo/Na-TiO_2(B) in Figure 2d displays the homogeneous distribution of RuMo nanoparticles (~2.1 ± 0.4 nm). High resolution TEM (HRTEM) image in Figure 2e shows the lattice fringe of 2.06 nm for the nanoparticle, corresponding to the Ru (101) lattice plane. Besides, numerous lattice distortions are found in the substrate including line defects, point defects and amorphous structure (Figures 2e-g and Figure S7). The elongated diffraction dots in

selected area electron diffraction (SAED) verify the defective structure in Na-TiO_2(B)[15]. However, TiO_2(B) nanobelts without caged Na^+ possess better crystallinity and less defects than Na-TiO_2(B) (Figure S9). As the substrate, the loaded nanoparticles on TiO_2(B) are not uniform and agglomerate obviously (Figure S10), indicating the structure defects induced by caged Na^+ play as the nucleation sites to reduce the surface free energy of nanoparticles, thus promoting the uniform distribution[7a, 9a].

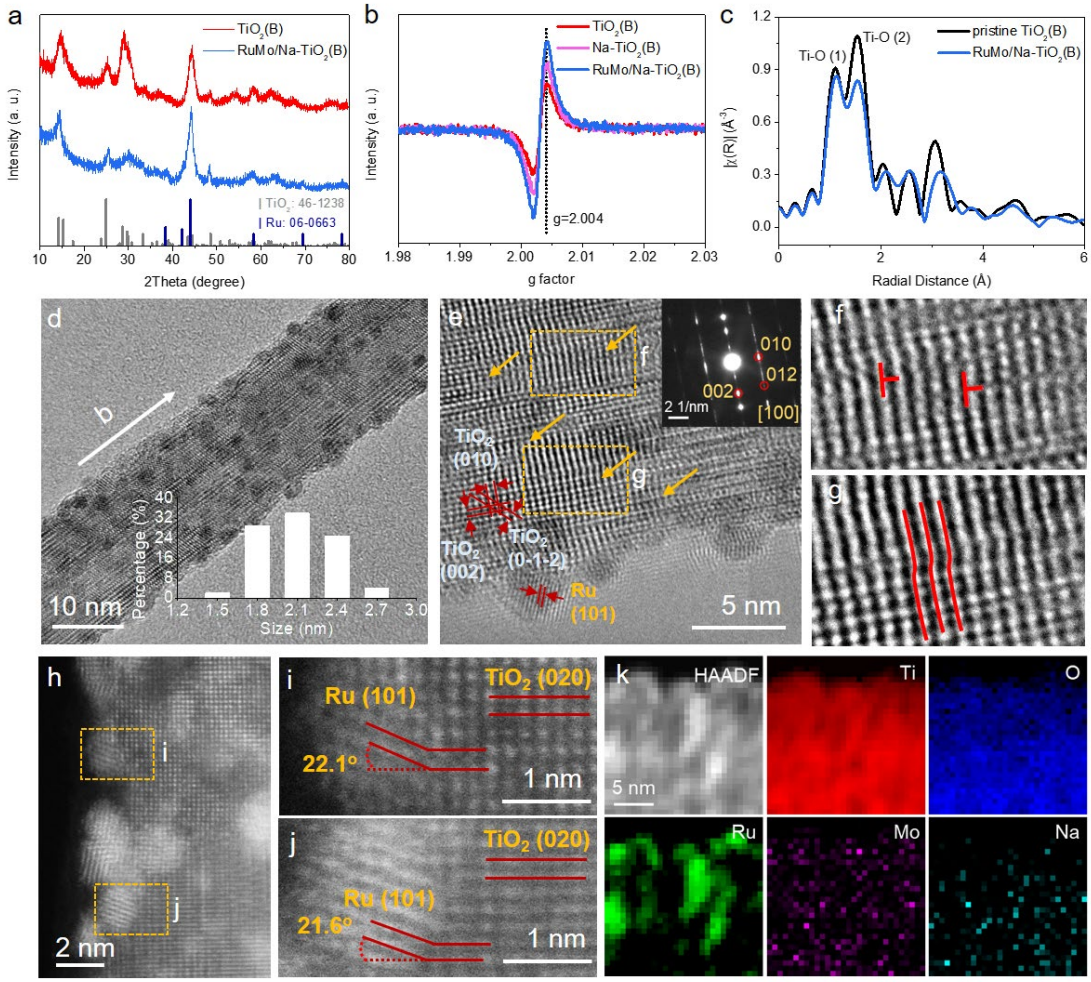

Figure 2. (a) XRD patterns of TiO_2(B) and RuMo/TiO_2(B). (b) EPR spectra of TiO_2(B), Na-TiO_2(B), and RuMo/Na-TiO_2(B). (c) Fourier transformed EXAFS of the Ti K-edge in R-space of pristine TiO_2(B) and RuMo/Na-TiO_2(B). (d) TEM image of RuMo/Na-TiO_2(B) (inset: the RuMo particle size distribution diagram). (e) HRTEM image of RuMo/Na-TiO_2(B), demonstrating numerous structural perturbations indicated by yellow arrows. The inset shows SAED pattern. (f, g) The enlarged parts in (e), showing

the edge dislocations (f) and screw dislocations (g). (h) HAADF-STEM image of RuMo/Na-TiO_2(B). (i, j) The enlarged parts in (h), indicating that Ru (101) grew along the (020) face of Na-TiO_2(B) with a certain angle of ~22°. (k) STEM-EELS mapping of RuMo/Na-TiO_2(B).

And high-angle annular dark-field imaging scanning transmission electron microscopy (HAADF-STEM) image demonstrates the Ru (101) grew along the TiO_2(B) (020) faces with a certain angle of ~22° due to the elimination of lattice mismatch (Figure 2h-j and Figure S11). Such directional bonding not only enhances the stability of nanoparticles, but also facilitates electron transfer in the heterojunction nanostructure[16]. The electron energy loss spectroscopy (EELS) mapping and energy dispersive X-ray (EDX) mapping at the atomic level further confirm the uniformly distributed Na^+ and uniform dispersion of RuMo alloys in the TiO_2(B) substrate (Figure 2k and Figure S12). Inductively coupled plasma optical emission spectrometer (ICP-OES) experiment confirms the mass contents of Ru, Mo and Na are 2.23, 0.17 and 3.32%, respectively.

2.2 Electronic structure analyses of RuMo/Na-TiO_2(B)

Subsequently, the localized electronic states of Ti, Ru and Mo in RuMo/Na-TiO_2(B) were investigated. As shown in the XPS spectra (Figure 3a), the Ti 2p in both RuMo/TiO_2(B) and RuMo/Na-TiO_2(B) exhibit a negative core level shift of 0.37 eV compared to that of TiO_2(B), indicating the strong interaction between RuMo alloy and TiO_2 support[16a]. The existence of Na–Ti–O signal was also proved by the Raman spectra (Figure S13)[17]. Moreover, the X-ray absorption near edge structure (XANES) spectra of Ti K-edge confirm caged Na^+ has little influence on the electronic structure of Ti (Figure 3b), which is consistent with the XPS result. In the pre-edge region of the Ti K-edge (inset of Figure 3b), Na-TiO_2(B) has a slightly higher intensity, suggesting the d-state of Ti in Na-TiO_2(B) is less filled, which could be caused by the presence of more O_V (Figure S14).

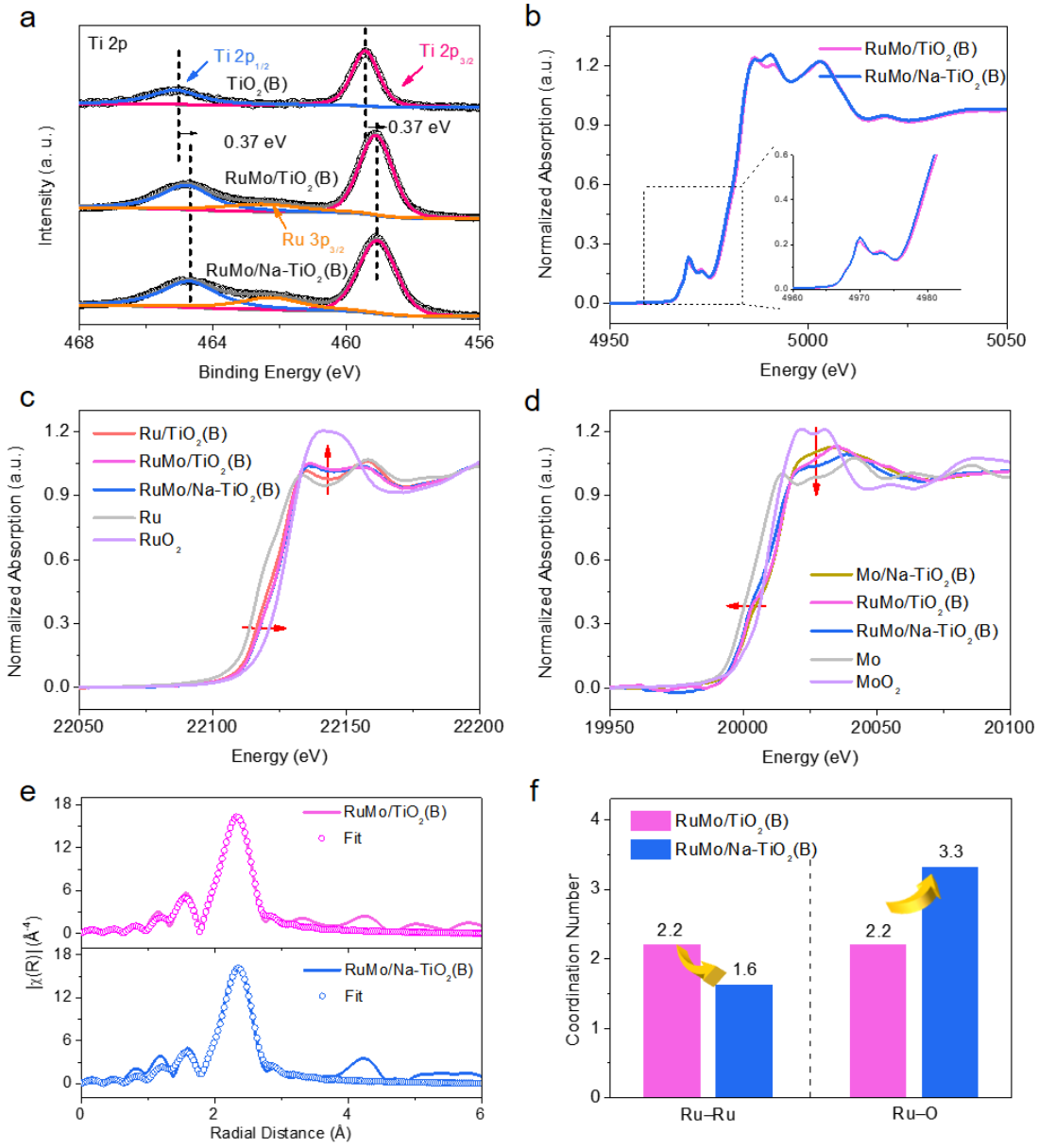

Figure 3. (a) XPS spectra of the Ti 2p of TiO_2(B), RuMo/TiO_2(B), and RuMo/Na-TiO_2(B). (b) XANES of the Ti K-edge of RuMo/TiO_2(B) and RuMo/Na-TiO_2(B). (c) XANES of the Ru K-edge of Ru/TiO_2(B), Ru/Na-TiO_2(B), RuMo/Na-TiO_2(B) and other references. (d) XANES of the Mo K-edge of Mo/Na-TiO_2(B), RuMo/TiO_2(B), RuMo/Na-TiO_2(B) and other references. (e) Fourier transformed EXAFS of the Ru K-edge in R-space for RuMo/TiO_2(B), RuMo/Na-TiO_2(B) and corresponding fitting curves. (f) Fitted Ru–Ru and Ru–O coordination number from EXAFS for RuMo/TiO_2(B) and RuMo/Na-TiO_2(B).

The electronic structure of RuMo alloy was also investigated. The adsorption edge

of RuMo/Na-TiO_2(B) sits between the one of metal and metal oxides, suggesting the Ru and Mo in these materials are in the slightly oxidized states. This may be ascribed to the under-coordinated edge and corner atoms in the nanoparticle and the support effect from Na-TiO_2(B). Compared to Ru/Na-TiO_2(B), the adsorption edge of Ru K-edge for RuMo/Na-TiO_2(B) slightly shifts to the higher energy (Figure 3c). Meanwhile, the adsorption edge of Mo K-edge for RuMo/Na-TiO_2(B) shifts to the lower energy compared to Mo/Na-TiO_2(B) (Figure 3d). Above results suggest the electron transfer from Ru to Mo in the nanoparticle. The downshift of the p-band center could promote the optimization of hydrogen intermediate adsorption of Ru during alkaline HER[18]. The EXAFS of the Ru K-edge in R-space exhibits a shell at 2.33 Å (Figure 3e), corresponding to the Ru–Ru scattering path in RuMo/TiO_2(B) and RuMo/Na-TiO_2(B). The fitted Ru–Ru coordination number (CN) in RuMo/Na-TiO_2(B) is 1.6, lower than the 2.2 of RuMo/TiO_2(B). RuMo/Na-TiO_2(B) also shows a larger Ru–O CN of 3.3 than that of RuMo/TiO_2(B) (Figure 3f and Table S2), suggesting the defective substrate can stabilize the nanoparticle with the smaller size. As for the Mo K-edge in R-space, RuMo/Na-TiO_2(B) shows the Mo–Ru shell at 2.27 Å while Mo–Mo interaction is absent in Mo/Na-TiO_2(B) (Figure S15b). According to the fitting results, only Mo–O bonds exist in Mo/Na-TiO_2(B) (Figure S17 and Table S3), indicating that there is no Mo particle in the Mo/Na-TiO_2(B). It is also confirmed by TEM observation (Figure S18). These results suggest Mo can only be reduced together with Ru. Such phenomenon was always reported in the electroplate to form Co/Ni-W alloys by co-deposition[19].

2.3 Electrocatalytic HER performance

The HER activity of RuMo/Na-TiO_2(B) was evaluated by the linear sweep voltammetry scans in alkaline electrolyte. It exhibits low overpotentials of 12 and 27 mV at the current density of 10 and 50 mA cm^{-2} (Figure 4a), respectively, superior to Pt/C with overpotentials of 29 mV (at 10 mA cm^{-2}) and 83 mV (at 50 mA cm^{-2}). Such low overpotentials indicate RuMo/Na-TiO_2(B) is a promising catalyst with high activity and low cost to replace Pt/C for HER. Besides, Mo/Na-TiO_2(B) shows the poor activity,

which means that Ru is the key active site (Figure S19a). The electrochemical performance of Ru/Na-TiO_2(B) is inferior to RuMo/Na-TiO_2(B), demonstrating the weakened hydrogen adsorption ability in RuMo alloy. It could be confirmed by the H_2-TPD experiments, showing the hydrogen desorption temperature at 148.4 ℃ for Ru and 118.8 ℃ for RuMo alloy (Figure S19b). The optimized hydrogen adsorption ability could favor the HER process. And the Tafel slope of RuMo/Na-TiO_2(B) is only 19.2 mV dec^{-1} (Figure 4b), much lower than those of Pt/C (31.9 mV dec^{-1}) and RuMo/TiO_2(B) (38.1 mV dec^{-1}), confirming the fast HER kinetics of RuMo/Na-TiO_2(B). To investigate the intrinsic hydrogen-evolving activity, TOF was calculated for comparison (Figure S20). The TOFs of RuMo/Na-TiO_2(B) are 3.9 times (at 20 mV overpotential) and 6.4 times (at 40 mV overpotential) of those of Pt/C, suggesting the high activity. Therefore, RuMo/Na-TiO_2(B) exhibits superior HER performance compared with other recently reported Ru-based catalysts (Figure 4d). Besides, the change of activity and structure of RuMo/Na-TiO_2(B) could be negligible after durable measurement, indicating the high stability (Figure 4e).

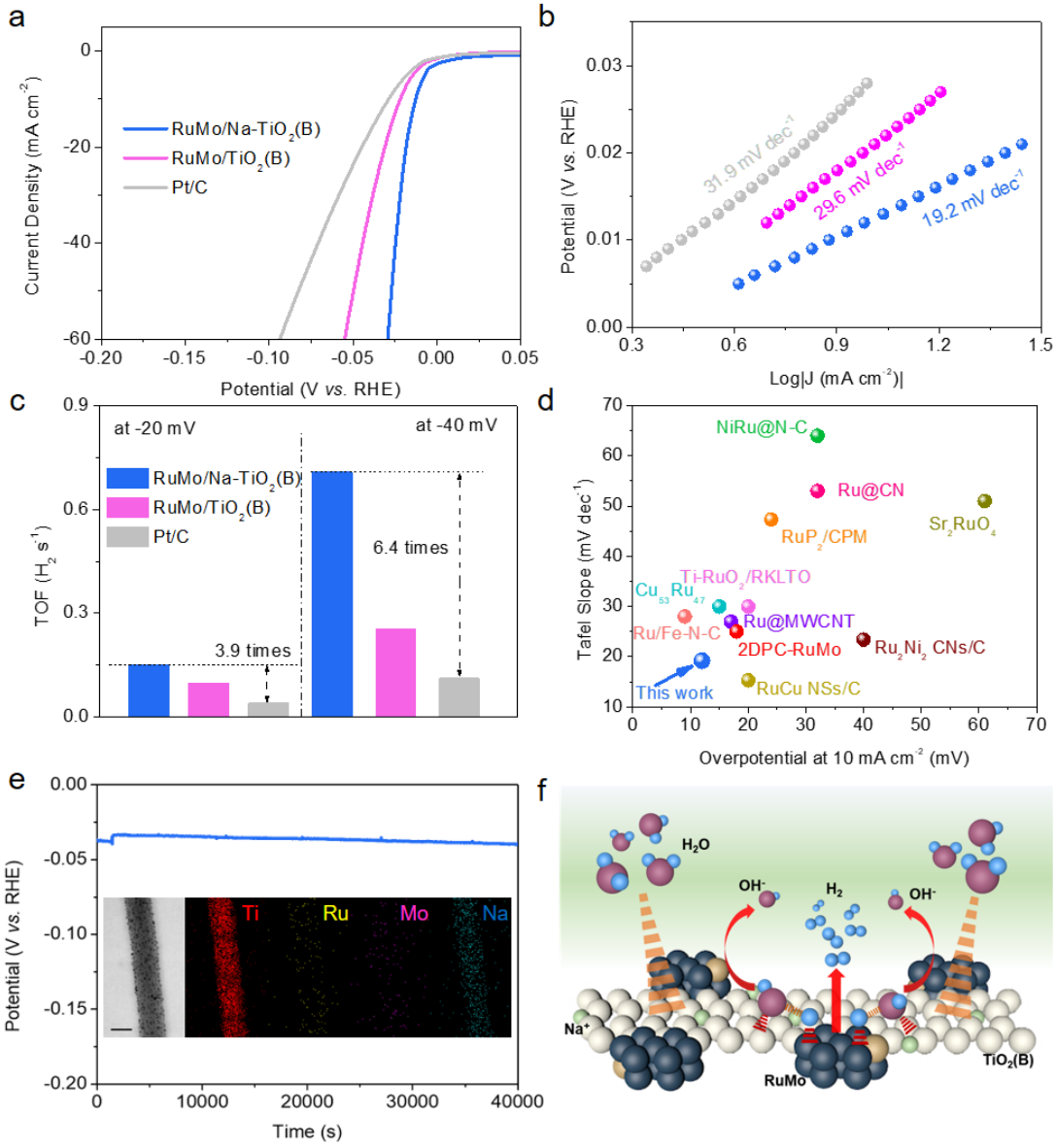

Figure 4. (a) Polarization curves of RuMo/Na-TiO_2(B), RuMo/TiO_2(B) and commercial Pt/C. (b) The corresponding Tafel plots from the curves in (a). (c) Comparison of TOF values for RuMo/Na-TiO_2(B), RuMo/TiO_2(B) and Pt/C. (d) Comparison of HER performance of RuMo/Na-TiO_2(B) with the state-of-the-art Ru-based HER electrocatalysts in alkaline solutions. (e) Stability measurement at the current density of 10 mA cm^{-2} for RuMo/Na-TiO_2(B). The inset shows the TEM-EDX mapping after stability measurement. Scale bar: 20 nm. (f) Schematic drawing for alkaline HER process on RuMo/Na-TiO_2(B).

To explore the HER mechanism on the RuMo/Na-TiO_2(B), the activity in an acidic

electrolyte was also performed. The overpotential and Tafel slope show obvious increase in acid solution, which are opposite to Pt/C (Figure S21). Compared to the acidic HER, the alkaline HER involves the additional water dissociation step of the H–OH bond cleaving (Volmer step). Therefore, the alkaline activity depends on the abilities of the water dissociation and hydrogen adsorption. With the decoration of caged Na^+, the water contact angles for Na-TiO_2(B) decreases to only 10.6° (Figure S22), indicating the strong water adsorption ability[20]. Such nanostructure in a OH^--rich electrolyte was confirmed to accelerate the water dissociation and provide a large amount of H^+ within the electric double layer, resulting in an acid-like micro-environment[21]. Thus, the alkaline HER on RuMo/Na-TiO_2(B) may obey the following steps: (i) The Na-TiO_2(B) substrate favors the water adsorption; (ii) The H–OH of water is cleaved at the boundary between lattice-distorted substrate and RuMo nanoparticle; (iii) OH^- desorption from the substrate is followed by adsorption of another water molecule and the resulting H^+ transfers on the surface of Ru forming the adsorbed H; (iv) The adsorbed H combines together to release hydrogen molecule (Figure 4f).

3. Conclusion

In conclusion, we prepared the heterojunction nanostructure of RuMo nanoparticles anchored on the bronze titanium dioxide (TiO_2(B) nanobelts with high density of lattice distortion and structural perturbations, showing high alkaline hydrogen evolution activity. The caged Na^+ not only induces structure defects into the nanobelts to stabilize and confine the metal nanoparticles, but also enhance the hydrophilia of the substrate to facilitate the water adsorption and dissociation. In alkaline solution, RuMo/Na-TiO_2(B) showed a low overpotential of 12 mV (at 10 mA cm^{-2}) and a small Tafel slope of 19.2 mV dec^{-1}, superior to the commercial Pt/C catalyst. And the combination of Na-TiO_2(B) nanobelt and RuMo nanoparticle facilitated the concerted effect in the multi-step HER. This work provides deep understanding of caged alkali cations-induced lattice distortion to anchor active nanoparticles for synergistically boosting the multi-step catalytic reactions.

Acknowledgements

The authors are grateful to the financial support from the National Natural Science Foundation of China (92163117, 52072389) and Shanghai Science and Technology Innovation Action Plan (20dz1204400). J. W. thanks the Program of Shanghai Academic Research Leader (20XD1424300) for financial support. L. L. acknowledges the support from the Discovery Program by the Natural Sciences and Engineering Research Council Canada (NSERC, DG RGPIN-2020-06675). Y. Z. thanks the support from the Research Grants Council of Hong Kong (C5029-18E) and the Hong Kong Polytechnic University grant (No. ZVRP). Technical supports from Dr. Debora Meira at the Advanced Photon Source, and Dr. Mohsen Shakouri at the Canadian Light Source are greatly appreciated.

Reference

[1] a) D. Zhao, Y. Wang, C.-L. Dong, Y.-C. Huang, J. Chen, F. Xue, S. Shen, L. Guo, *Nat. Energy* **2021**, *6*, 388-397; b) M. Luo, W. Sun, B. B. Xu, H. Pan, Y. Jiang, *Adv. Energy Mater.* **2021**, *11*, 2002762; c) Y. Zhou, E. Song, W. Chen, C. U. Segre, J. Zhou, Y. C. Lin, C. Zhu, R. Ma, P. Liu, S. Chu, T. Thomas, M. Yang, Q. Liu, K. Suenaga, Z. Liu, J. Liu, J. Wang, *Adv. Mater.* **2020**, *32*, 2003484; d) Y. P. Li, J. H. Zhang, Y. Liu, Q. Z. Qian, Z. Y. Li, Y. Zhu, G. Q. Zhang, *Sci. Adv.* **2020**, *6*, eabb4197.

[2] a) M. Wang, Y. Xu, C.-K. Peng, S.-Y. Chen, Y.-G. Lin, Z. Hu, L. Sun, S. Ding, C.-W. Pao, Q. Shao, X. Huang, *J. Am. Chem. Soc.* **2021**, *143*, 16512; b) B. Zhao, Z. Wan, Y. Liu, J. Xu, X. Yang, D. Shen, Z. Zhang, C. Guo, Q. Qian, J. Li, R. Wu, Z. Lin, X. Yan, B. Li, Z. Zhang, H. Ma, B. Li, X. Chen, Y. Qiao, I. Shakir, Z. Almutairi, F. Wei, Y. Zhang, X. Pan, Y. Huang, Y. Ping, X. Duan, X. Duan, *Nature* **2021**, *591*, 385; c) Z. Weng, W. Liu, L.-C. Yin, R. Fang, M. Li, E. I. Altman, Q. Fan, F. Li, H.-M. Cheng, H. Wang, *Nano Lett.* **2015**, *15*, 7704.

[3] a) R. Li, H. Wang, F. Hu, K. C. Chan, X. Liu, Z. Lu, J. Wang, Z. Li, L. Zeng, Y. Li, X. Wu, Y. Xiong, *Nat. Commun.* **2021**, *12*, 3540; b) T. Gan, J. Yang, D. Morris, X. Chu, P. Zhang, W. Zhang, Y. Zou, W. Yan, S.-H. Wei, G. Liu, *Nat. Commun.* **2021**, *12*, 2741; c) D. Zhao, K. Sun, W.-C. Cheong, L. Zheng, C. Zhang, S. Liu, X. Cao, K. Wu, Y. Pan, Z. Zhuang, B. Hu, D. Wang, Q. Peng, C. Chen, Y. Li, *Angew. Chem. Int. Ed.* **2020**, *59*, 8982; d) Y. Zhang, W. Yan, H. Qi, X. Su, Y. Su, X. Liu, L. Li, X. Yang, Y. Huang, T. Zhang, *ACS Catal.* **2022**, *12*, 1697.

[4] a) Y. Jia, K. Jiang, H. Wang, X. Yao, *Chem* **2019**, *5*, 1371; b) Y. Tang, C. Yang, X. Xu, Y. Kang, J. Henzie, W. Que, Y. Yamauchi, *Adv. Energy Mater.* **2022**, *12*, 2103867.

[5] a) Y. Yao, S. Hu, W. Chen, Z.-Q. Huang, W. Wei, T. Yao, R. Liu, K. Zang, X. Wang, G. Wu, W. Yuan, T. Yuan, B. Zhu, W. Liu, Z. Li, D. He, Z. Xue, Y. Wang, X. Zheng, J. Dong, C.-R. Chang, Y. Chen, X. Hong, J. Luo, S. Wei, W.-X. Li, P. Strasser, Y. Wu, Y. Li, *Nat. Catal.* **2019**, *2*, 304; b) S. Maiti, K. Maiti, M. T. Curnan, K. Kim, K.-J. Noh, J. W. Han, *Energy Environ. Sci.* **2021**, *14*, 3717; c) W. Zang, T. Sun, T. Yang, S. Xi, M. Waqar, Z. Kou, Z. Lyu, Y. P. Feng, J. Wang, S. J. Pennycook, *Adv. Mater.* **2021**, *33*, 2003846; d) S. Zhang, Y. Si, B. Li, L. Yang, W. Dai, S. Luo, *Small* **2021**, *17*, 2004980; e) G. Lin, Q. Ju, Y. Jin, X. Qi, W. Liu, F. Huang, J. Wang, *Adv. Energy Mater.* **2021**, *11*, 2101050.

[6] W. Huang, C. Johnston-Peck Aaron, T. Wolter, D. Yang Wei-Chang, L. Xu, J. Oh, A. Reeves Benjamin, C. Zhou, E. Holtz Megan, A. Herzing Andrew, M. Lindenberg Aaron, M. Mavrikakis, M. Cargnello, *Science* **2021**, *373*, 1518.

[7] a) C. Zhang, F. Liu, Y. Zhai, H. Ariga, N. Yi, Y. Liu, K. Asakura, M. Flytzani-Stephanopoulos, H. He, *Angew. Chem. Int. Ed.* **2012**, *51*, 9628; b) J. A. Rodriguez, D. C. Grinter, P. J. Ramírez, D. J. Stacchiola, S. Senanayake, *J. Phys. Chem. C* **2018**, *122*, 4324.

[8] a) L. Xue, H. He, C. Liu, C. Zhang, B. Zhang, *Environ. Sci. Technol.* **2009**, *43*, 890; b) J. R. Jokisaari, D. Bayerl, K. Zhang, L. Xie, Y. Nie, D. G. Schlom, E. Kioupakis, G. W. Graham, X. Pan, *Chem. Mater.* **2015**, *27*, 7896.

[9] a) Y. B. Li, C. B. Zhang, H. He, J. H. Zhang, M. Chen, *Catal. Sci. Technol.* **2016**, *6*, 2289; b) E. Khorashadizade, S. Mohajernia, S. Hejazi, H. Mehdipour, N. Naseri, O. Moradlou, N. Liu, A. Z. Moshfegh, P. Schmuki, *ChemElectroChem* **2020**, *7*, 1699.

[10] Y. Zhai, D. Pierre, R. Si, W. Deng, P. Ferrin, U. Nilekar Anand, G. Peng, A. Herron Jeffrey, C. Bell David, H. Saltsburg, M. Mavrikakis, M. Flytzani-Stephanopoulos, *Science* **2010**, *329*, 1633.

[11] Y. Zhang, Z. Ding, C. W. Foster, C. E. Banks, X. Qiu, X. Ji, *Adv. Funct. Mater.* **2017**, *27*.

[12] H. Hirakawa, M. Hashimoto, Y. Shiraishi, T. Hirai, *J. Am. Chem. Soc.* **2017**, *139*, 10929.

[13] L. J. Zhang, H. Jang, H. H. Liu, M. G. Kim, D. J. Yang, S. G. Liu, X. E. Liu, J. Cho, *Angew. Chem. Int. Ed.* **2021**, *60*, 18821.

[14] X. Chen, L. Liu, F. Huang, *Chem. Soc. Rev.* **2015**, *44*, 1861.

[15] a) L. Qiao, Q. L. Feng, *J. Cryst. Growth* **2007**, *304*, 253; b) M. M. J. Treacy, J. M. Newsam, M. W. Deem, *Ultramicroscopy* **1993**, *52*, 512.

[16] a) Y. Zhou, Z. Xie, J. Jiang, J. Wang, X. Song, Q. He, W. Ding, Z. Wei, *Nat. Catal.* **2020**, *3*, 454; b) T.-N. Ye, S.-W. Park, Y. Lu, J. Li, M. Sasase, M. Kitano, T. Tada, H. Hosono, *Nature* **2020**, *583*, 391.

[17] Y. V. Kolen'ko, K. A. Kovnir, A. I. Gavrilov, A. V. Garshev, J. Frantti, O. I. Lebedev, B. R. Churagulov, G. Van Tendeloo, M. Yoshimura, *J. Phys. Chem. B* **2006**, *110*, 4030.

[18] K. Tu, D. Tranca, F. Rodríguez-Hernández, K. Jiang, S. Huang, Q. Zheng, M. X. Chen, C. Lu, Y. Su, Z. Chen, H. Mao, C. Yang, J. Jiang, H. W. Liang, X. Zhuang, *Adv. Mater.* **2020**, *32*, 2005433.

[19] a) U. Admon, M. P. Dariel, E. Grünbaum, *J. Appl. Phys.* **1986**, *59*, 2002; b) E. Gileadi, N. Eliaz, *ECS Trans.* **2007**, *2*, 337.

[20] Q. Xu, H. Jiang, X. Duan, Z. Jiang, Y. Hu, S. W. Boettcher, W. Zhang, S. Guo, C. Li, *Nano Lett.* **2020**, *21*, 429.

[21] a) X. Wang, C. Xu, M. Jaroniec, Y. Zheng, S.-Z. Qiao, *Nat. Commun.* **2019**, *10*, 4876; b) Y.-H. Wang, S. Zheng, W.-M. Yang, R.-Y. Zhou, Q.-F. He, P. Radjenovic, J.-C. Dong, S. Li, J. Zheng, Z.-L. Yang, G. Attard, F. Pan, Z.-Q. Tian, J.-F. Li, *Nature* **2021**, *600*, 81.